Electronic Structure

OPEN ACCESS

TECHNICAL NOTE

MARMOT: magnetism, anisotropy, and more, using the relativistic disordered local moment picture at finite temperature

Christopher E Patrick[1,*] and Julie B Staunton[2]

[1] Department of Materials, University of Oxford, Oxford OX1 3PH, United Kingdom
[2] Department of Physics, University of Warwick, Coventry CV4 7AL, United Kingdom
[*] Author to whom any correspondence should be addressed.

E-mail: christopher.patrick@materials.ox.ac.uk and j.b.staunton@physics.warwick.ac.uk

Keywords: magnetism, anisotropy, density-functional theory, disordered local moments

RECEIVED
7 December 2021

REVISED
11 February 2022

ACCEPTED FOR PUBLICATION
22 February 2022

PUBLISHED
9 March 2022

Abstract

We present MARMOT, a hybrid Python/FORTRAN implementation of the disordered local moment picture within multiple scattering density-functional theory. MARMOT takes atom-centred, scalar-relativistic potentials and constructs an effective medium (within the coherent potential approximation) to describe the disordered magnetic moment orientations at finite temperature. By solving the single-site scattering problem fully relativistically, spin–orbit effects are included, allowing the magnetocrystalline anisotropy to be calculated. Magnetic transition temperatures, spin and orbital moments, the density-of-states, and analytical parameterizations of the magnetic potential energy surface can also be calculated. Here, we describe the theory and practical implementation of MARMOT, and demonstrate its use by calculating Curie temperatures, magnetizations and anisotropies of bcc Fe, $GdFe_2$ and YCo_5.

1. Introduction

Magnetism and magnetic materials lie at the heart of numerous areas of scientific research. In addition to fundamental studies of exotic phenomena [1–3], the possibilities for applied magnetism research are wide-ranging, tackling topical questions regarding data storage, energy generation, mobility, refrigeration, spintronics and quantum computing [4–6]. Computational research makes an important contribution to this field, whether by exploring and predicting the properties of new materials, or by interpreting experimental observations [7, 8].

One of the interesting features of magnetism is that its characteristic energy scale is comparable to that associated with thermal excitations. As a result, a material's magnetic properties change dramatically with the temperature T of its environment. The most well-known example of this is the Curie temperature, where a ferromagnet loses its intrinsic magnetism above a critical temperature T_C. More generally, changing the temperature can trigger transitions between different magnetic phases, possibly accompanied by structural changes [9]. Other examples of temperature-dependent magnetic phenomena include the loss of coercivity with heating [10], zero thermal-expansion (invar) behaviour [11], and magnetization switching in compensated ferrimagnets [12].

From a computational perspective, accounting for the effects of temperature creates an additional layer of complexity on top of the other challenges already associated with describing magnetism. For real-time simulations, thermal effects can be accounted for by coupling to a thermostat, which may or may not take into account the quantum nature of the magnetic excitations [13]. Alternatively, statistical mechanics provides a framework to calculate the properties of a material at thermal equilibrium. In the case that the magnetism can be understood in terms of a specific part of the material interacting with its environment, (e.g. a magnetic fragment surrounded by a host), the methods of dynamical mean-field theory can be used to obtain the excitation spectrum and partition function of that fragment, and therefore its temperature-dependent properties [14].

However, for a large collection of magnetic moments the phase space spanned by the possible excitations is prohibitively large.

One viable option is to map the complicated magnetic interactions onto a simpler model (e.g. the Heisenberg model), whose finite temperature behaviour is known or can be obtained computationally. Such models require input parameters to describe the strength of the interactions, which might be taken from first-principles calculations based on density-functional theory (DFT) or extracted from experimental data [15–17]. However, it is important to realise that the first-principles calculations are themselves being performed at a specific temperature; usually at absolute zero (perfect magnetic order), or possibly in the paramagnetic state (full disorder) [18]. Obtaining the electronic and magnetic structure of a material for $0 < T < T_C$ from first principles requires simulating a partially-ordered magnetic material, and this is a challenging problem [19, 20].

The disordered local moment (DLM) picture provides a theoretical and conceptual framework to understand the electronic structure of magnetic materials in this temperature regime. In particular, Györffy *et al* formulated DLM in terms of DFT to make a quantitative theory [21]. The theory describes the magnetic order within a mean-field approach, whereby the local magnetic moments at each atomic site influence, and are influenced by, the global magnetic order. The mechanism by which the order is established is not through pre-supposed (e.g. pairwise) magnetic interactions, but rather through the entire electronic structure of the material, as calculated through DFT. This means the calculations automatically include 'beyond-Heisenberg' exchange, e.g. higher-order and multi-site interactions [22]. Furthermore, the framework incorporates relativistic effects, so that magnetocrystalline anisotropy (MCA) and orbital moments can be calculated [23]. More generally, the theory provides a self-contained framework to calculate finite temperature magnetic properties at a similar cost, and at a consistent theoretical level, to DFT.

The Györffy formulation of DLM theory has found a number of applications over the years, and continues to be the subject of active research [24–31]. However, it has a small user base, especially within the context of the rapid growth of first-principles DFT calculations in other areas of materials science. There are two obvious ways of increasing the accessibility of these DLM calculations. The first is to note that up to now, software implementing the DLM equations has tended to remain in the developmental phase, so that a high level of expertise is required to run calculations. Packaging the software as a stable release, complete with examples, documentation, and benchmarks, would address this issue. The second way notes that DLM theory is implemented as an additional, post-processing step on top of a previous DFT calculation. There is huge potential to widen the DLM user base by putting in place a framework to interface DLM with the many high-quality, user-friendly DFT software packages which are now available [32].

With these aspects in mind, we have developed a software package which implements the DLM theory of reference [21] and its subsequent modifications. The package calculates **M**agnetism, **A**nisotropy, and more, using the **R**elativistic disordered local **MO**ment picture at finite **T**emperature (`MARMOT`). The guiding principle has been to keep the user interface simple and intuitive whilst maintaining good underlying performance for the most computationally-intensive part of the calculation. We achieve this by coding the high intensity routines in `FORTRAN` and placing them within a `Python` wrapper. The resulting software achieves the desired improvements both in performance and usability, and is now available as a new research tool for the computational magnetism community.

This manuscript has been written to accompany the newly-developed software. Section 2 describes the theory implemented in `MARMOT`. Section 3 explains the technical aspects involved in performing a calculation, and section 4 gives examples of the code in use. Section 5 concludes by outlining some directions for future development.

2. Theoretical background

2.1. Introduction

In this section we describe the DLM theory implemented in `MARMOT`, providing sufficient detail that the reader can understand the key steps, inputs and outputs of a typical calculation. We refer to published literature for discussion of the underlying theory and derivations. A careful and clear description of the fundamentals of DLM is given in reference [21]. The solution of the relativistic single-site scattering problem and the subsequent calculation of MCA is described in references [33–35], and the modification of the single-site equations to include the local self-interaction correction (LSIC) [36] and the orbital polarization correction (OPC) [37, 38] is described in reference [39]. More general discussion of multiple scattering theory and the Korringa–Kohn–Rostocker (KKR) formalism may be found e.g. in references [40–42].

2.2. Local moments

The primary quantities in DLM theory are the local (magnetic) moments. A local moment at site i corresponds to a region of spin polarization to which we can assign a magnetic moment of magnitude μ_i and direction $\hat{\vec{e}}_i$.

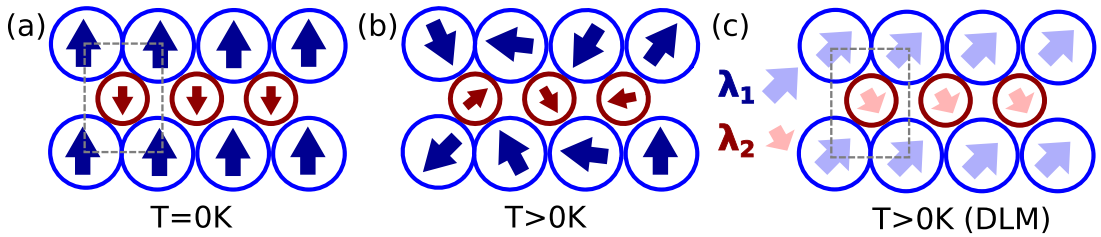

Figure 1. An illustration of the DLM concept for a ferrimagnet with two magnetic sublattices. At zero temperature (a) the local moments form an ordered array, with a periodic unit cell shown as the dashed box. At finite temperature (b) the local moment orientations fluctuate, such that a particular snapshot shows disorder and the spatial periodicity is lost. DLM theory (c) restores this periodicity by focusing on the time-averaged orientation of these moments, quantified by the beta-h quantities $\{\vec{\lambda}_i\}$.

Local moments can originate both from localized and delocalized (itinerant) electrons. In the latter case, it is the scattering of the itinerant electrons at atomic sites which polarizes the environment, setting up regions of magnetization which we identify as the local moments [21].

For most magnetic materials, at zero temperature the local moments form an ordered array (e.g. ferromagnetic, antiferromagnetic, ferrimagnetic) corresponding to their lowest energy state, as shown in figure 1(a). Figure 1(b) illustrates how raising the temperature introduces fluctuations in the magnetic order, such that the material can access higher-energy microstates with DLM orientations. In the theory implemented in MARMOT, we consider only fluctuations in the local moment directions $\vec{e}_i$ and not the longitudinal fluctuations in their magnitudes μ_i. As such, we must limit the application of our theory to 'good' local moment systems, where the value of μ_i is independent of the global magnetic order of the material. As an approximate rule-of-thumb, local moments with the size of a Bohr magneton or greater ($> \sim 1\ \mu_B$) at zero temperature tend to retain their magnitude as the temperature is increased, and therefore can be considered 'good'.

2.3. The statistical mechanics of the local moments

DLM theory treats the fluctuations of the local moments classically, with the orientation vectors $\vec{e}_i$ able to take any direction on the unit sphere. A particular DLM microstate is described through a set of unit vectors $\{\vec{e}_i\}$, and the energy of the microstate is given by the grand potential, $\Omega(\{\vec{e}_i\})$. According to classical statistical mechanics, the probability of finding the material in this microstate is $P(\{\vec{e}_i\}) = \exp[-\beta\Omega(\{\vec{e}_i\})]/Z$, with the partition function $Z = \int d\vec{e}_1 d\vec{e}_2 \ldots \exp[-\beta\Omega(\{\vec{e}_i\})]$, and $\beta = 1/(k_B T)$ where T is the temperature and k_B is Boltzmann's constant. Further thermodynamic quantities are derived from the partition function, e.g. the Helmholtz energy $F = -k_B T \ln Z$.

DLM theory assumes that the grand potential $\Omega(\{\vec{e}_i\})$ can be calculated through constrained spin-density-functional theory [21]. In practice such a calculation would be very difficult, since $\{\vec{e}_i\}$ represents the orientations of all the local moments in the crystal (a huge number) compared to just in the crystallographic or magnetic unit cell. Accordingly, integrating over the entire phase space to obtain Z is intractable.

To proceed, we replace the 'true' statistical mechanics with an approximate version. An auxiliary grand potential Ω_0 is introduced with a prescribed analytical dependence on the local moments,

$$\Omega_0(\{\vec{e}_i\}) = -\sum_i \vec{h}_i \cdot \vec{e}_i. \tag{1}$$

The vector quantities $\{\vec{h}_i\}$ are referred to as Weiss fields (although strictly, they have dimensions of energy). They describe the magnetic field felt by each local moment, with large Weiss fields corresponding to a high degree of magnetic order. It is convenient to introduce the lambda or 'beta-h' quantities $\vec{\lambda}_i = \beta\vec{h}_i$, and also the direction unit vector $\hat{n}_i$, i.e. $\vec{\lambda}_i = \lambda_i \hat{n}_i$. The statistical mechanics of the auxiliary system can be solved analytically, with the probability factorising into single-site functions: $P_0(\{\vec{e}_i\}) = \prod_i P_{0i}(\vec{e}_i)$, where

$$P_{0i}(\vec{e}_i) = \frac{\exp[\vec{\lambda}_i \cdot \vec{e}_i]}{(4\pi/\lambda_i)\sinh\ \lambda_i}. \tag{2}$$

The order parameter for each local moment $\vec{m}_i$ is obtained as $\langle\vec{e}_i\rangle_{0,T}$, where $\langle\rangle_{0,T}$ denotes a thermal average with respect to the auxiliary system:

$$\begin{aligned}\vec{m}_i &= \int d\vec{e}_i P_{0i}(\vec{e}_i)\vec{e}_i \prod_{j\neq i} \int d\vec{e}_j P_{0j}(\vec{e}_j) \\ &= L(\lambda_i)\hat{n}_i,\end{aligned} \tag{3}$$

where $L(\lambda_i)$ is the Langevin function, $L(\lambda_i) = 1/\tanh\lambda_i - 1/\lambda_i$. Equation (3) shows how the magnitudes and directions of the order parameters are fixed by the Weiss fields, and also how small 'beta-h' values correspond to a low degree of magnetic order, i.e. high temperature.

The true and the auxiliary systems are linked by the thermodynamic inequality satisfied by the Helmholtz energy [43]: $F(T) \leqslant \mathcal{F}(\mathcal{T})$, where

$$\mathcal{F}(T) = F_0(T) - \langle\Omega_0\rangle_{0,T} + \langle\Omega\rangle_{0,T}. \tag{4}$$

$F_0(T)$ is the Helmholtz energy of the auxiliary system. The inequality allows us to define the 'best' Weiss fields as those which minimize $\mathcal{F}(\mathcal{T})$, the upper bound to the true free energy $F(T)$. Setting $\nabla_{\vec{h}_i}\mathcal{F} = 0$ yields two equivalent expressions satisfied by these Weiss fields:

$$\vec{h}_i = -\nabla_{\vec{m}_i}\langle\Omega\rangle_{0,T} = -\frac{3}{4\pi}\int \mathrm{d}\vec{\hat{e}}_i \langle\Omega\rangle_{0,T}^{\vec{\hat{e}}_i}\,\vec{\hat{e}}_i \tag{5}$$

where the notation $\langle\rangle_{0,T}^{\vec{\hat{e}}_i}$ describes a thermal average over all local moment orientations except the ith moment, which is held at the orientation $\vec{\hat{e}}_i$.

Equation (5) provides the critical relationship between the tendency of the local moments to order (fixed by the Weiss field, through equation (3)), the temperature T, and the magnetic grand potential Ω. For example, for a ferromagnet we expect nonzero solutions of equation (5) only for $T < T_C$. We note that equation (5) involves an implicit self-consistency, because the thermal average on the right-hand side depends on the probability, which is fixed by the Weiss fields. This aspect is discussed further in section 3.6.

2.4. Scattering theory treatment of disorder

The key quantity in equation (5) is $\langle\Omega\rangle_{0,T}$: the average energy of a system, where the probability of finding a local moment pointing along $\vec{\hat{e}}_i$ is independent of the orientations of all other moments, and is proportional to $\exp[\vec{\lambda}_i \cdot \vec{\hat{e}}_i]$. Figure 1(c) provides a physical picture of this situation. The faint arrows can be thought of representing either the averaged local moment orientation $\vec{m}_i$, the Weiss field $\vec{h}_i$ or the beta-h value $\vec{\lambda}_i$; all are related through equation (3). Unlike the snapshot of the microstate [figure 1(b)], this representation is expected to exhibit translational symmetry.

DLM theory exploits the analogy between the magnetically-disordered system of figure 1(c) and a compositionally-disordered random alloy of different elements. A natural framework to calculate the electronic structure of such an alloy is the multiple-scattering, KKR formalism combined with the coherent potential approximation (CPA) [40–42]. In the multiple-scattering picture, electrons travel freely through the crystal until they reach an atomic site, where they are scattered and sent off in a new direction. There are two parts to the problem. The first is the single site scattering, which considers how an electron interacts with the isolated atomic site. The key quantity obtained from solving this part of the problem is the t-matrix, which is a matrix in spin and orbital angular momentum quantum numbers $L = (lm\sigma)$. In MARMOT we calculate $\underline{t}_i(\vec{z}, E)$, which describes the scattering of an electron of energy E off the atom at site i whose local moment (i.e. spin quantization axis) is pointing along the z axis. It is straightforward to transform this matrix to an arbitrary local moment orientation $\underline{t}_i(\vec{\hat{e}}_i) = \underline{R}(\vec{\hat{e}}_i)\underline{t}_i(\vec{z})\underline{R}^\dagger(\vec{\hat{e}}_i)$ where $\underline{R}$ is a suitable rotation matrix. As discussed in section 2.8, MARMOT can solve the scattering problem fully-relativistically so that spin–orbit effects are naturally included, or in scalar- or non-relativistic approximations.

The second part of the problem incorporates the electron's entire path through the crystal. The structure constant matrix $\underline{\underline{G}}_0(E)$ describes free electron propagation, projected onto spin and angular functions located at different sites. As emphasised by the double underline it is a supermatrix, with $\underline{\underline{G}}_{0_{ij}}$ describing propagation between sites i and j projected onto the L basis. The free propagation and single-site scattering combine to form the scattering path operator $\underline{\underline{\tau}}(E)$,

$$\underline{\underline{\tau}}(E) = \left[\underline{\underline{t}}^{-1}(E) - \underline{\underline{G}}_0(E)\right]^{-1}, \tag{6}$$

where the t-supermatrix is formed as $\underline{\underline{t}}_{ij} = \delta_{ij}\underline{t}_i$. The energies where the scattering path operator is singular correspond to the energy eigenstates of the material [40].

The key idea of the CPA is to construct an effective medium whose site-diagonal elements of the scattering path operator reproduce those of the true τ, on average. This is achieved in practice by assigning an effective t matrix to each site in the magnetic unit cell, $\underline{t}_{c,i}$. The translational symmetry of the effective medium modifies the matrix inversion in equation (6), to

$$\underline{\underline{\tau}}_c(E) = \frac{V_c}{(2\pi)^3}\int_{\mathrm{BZ}} \mathrm{d}\vec{k}\left[\underline{\underline{t}}_c^{-1}(E) - \underline{\underline{G}}_0(E,\vec{k})\right]^{-1}, \tag{7}$$

where 'BZ' refers to the first Brillouin zone, and V_c is the volume of the real-space unit cell which contains the sites i. The CPA places the following condition on the site-diagonal elements of this matrix ($\underline{\tau_{c,ii}} = \underline{\underline{\tau_c}}_{ii}$) which must hold for every site [35]:

$$\underline{\tau_{c,ii}} = \int \mathrm{d}\vec{\hat{e}}_i P_{0i}(\vec{\hat{e}}_i)\underline{\tau_{c,ii}}\,\underline{D_i}(\vec{\hat{e}}_i) \tag{8}$$

where (dropping the energy dependence for clarity)

$$\underline{D_i}(\vec{\hat{e}}_i) = \left[\underline{1} + \left(\underline{t_i}^{-1}(\vec{\hat{e}}_i) - \underline{t_{i,c}^{-1}}\right)\underline{\tau_{c,ii}}\right]^{-1}. \tag{9}$$

An alternative statement of the CPA condition makes use of the excess scattering matrices X, and states that $\underline{X_{ci}} = 0$, where

$$\underline{X_{ci}} = \int \mathrm{d}\vec{\hat{e}}_i P_{0i}(\vec{\hat{e}}_i)\underline{X_i}(\vec{\hat{e}}_i) \tag{10}$$

and

$$\underline{X_i}(\vec{\hat{e}}_i) = \left[\left(\underline{t_{i,c}^{-1}} - \underline{t_i}^{-1}(\vec{\hat{e}}_i)\right)^{-1} - \underline{\tau_{c,ii}}\right]^{-1}. \tag{11}$$

These matrices form the basis of an iterative scheme to determine $\underline{t_{i,c}}$. Starting from an initial guess of the $\underline{t_{i,c}}$ matrices, equation (7) is used to calculate $\underline{\underline{\tau_c}}$. The excess scattering matrices are then calculated using equation (11). If $\underline{X_{ci}}$ does not equal zero as required by the CPA, the single-site $\underline{t_{i,c}}$ matrices are updated according to

$$\underline{t_{i,c}}^{\mathrm{New}} = \left[\underline{t_{i,c}}^{-1} - (1 + \underline{X_{ci}}\,\underline{\tau_{c,ii}})^{-1}\underline{X_{ci}}\right]^{-1}. \tag{12}$$

The convergence of the CPA is checked by comparing the traces of the $\underline{t_{i,c}}$ matrices between iterations. The initial guess of $\underline{t_{i,c}}$ is found from the average t-matrix approximation (ATA), $\underline{t_{i,c}}^{\mathrm{first}} = \int \mathrm{d}\vec{\hat{e}}_i P_{0i}(\vec{\hat{e}}_i)\underline{t_i}(\vec{\hat{e}}_i)$. In the course of the calculation, $\underline{t_{i,c}}$ and $\underline{\tau_{c,ii}}$ are updated, but the single-site matrices $\underline{t_i}$ do not change: `MARMOT` does not follow the self-consistent scheme demonstrated in reference [44], where the electron (spin) density calculated for the CPA medium is used to update $\underline{t_i}$.

Using the CPA to model disorder significantly reduces the computational effort compared to explicitly sampling many magnetic configurations in a supercell. The angular momentum expansions are performed up to a maximum orbital quantum number $l_{\max}$. Taking spin into account, this means matrices like $\underline{t_{i,c}}$ have a size of $\mathtt{nL} = 2(l_{\max}+1)^2$. For the typical case of $l_{\max} = 3$, this amounts to only a 32×32 matrix. Furthermore, the number of operations scales linearly with the number of sites in the unit cell, and as a result, the manipulations required to update the CPA medium do not carry a significant overhead. The most time-consuming part of the calculation is associated with equation (7). Assuming `nsub` sites in the unit cell, the supermatrices have sizes of `nsub` $\times$ `nL`, which in itself is not prohibitive for 1–100 sites. However, significant computational cost comes from evaluating the structure constants, and performing the matrix inversion at every $\vec{k}$-vector, the number of which can be large.

2.5. Compositional disorder

The above discussion assumed a single type of atom at each site, but the CPA framework naturally allows treatment of compositional disorder. Taking the concentration of atom type α at site i to be $c_{i\alpha}$, the CPA equations are modified as follows:

$$\begin{aligned}
\underline{t_{i,c}}^{\mathrm{first}} &= \sum_\alpha c_{i\alpha} \int \mathrm{d}\vec{\hat{e}}_i P_{0i\alpha}(\vec{\hat{e}}_i)\underline{t_{i\alpha}}(\vec{\hat{e}}_i) \\
\underline{X_{i\alpha}}(\vec{\hat{e}}_i) &= \left[\left(\underline{t_{i,c}^{-1}} - \underline{t_{i\alpha}}^{-1}(\vec{\hat{e}}_i)\right)^{-1} - \underline{\tau_{c,ii}}\right]^{-1} \\
\underline{X_{ci}} &= \sum_\alpha c_{i\alpha} \int \mathrm{d}\vec{\hat{e}}_i P_{0i\alpha}(\vec{\hat{e}}_i)\underline{X_{i\alpha}}(\vec{\hat{e}}_i)
\end{aligned} \tag{13}$$

Equations (7), (12) and (13) constitute the full set which must be solved in the general case of compositional and magnetic disorder. We note that the single-site probability P_0 carries an α subscript, because each atom type on each site feels a unique Weiss field $\vec{h}_{i\alpha}$, and therefore has its own beta-h value $\vec{\lambda}_{i\alpha}$.

2.6. Calculating the Weiss fields

Once the $\underline{t_{i,c}}$ matrices describing the CPA effective medium have been obtained, the calculation of magnetic properties proceeds via the Lloyd formula for the integrated density-of-states $N(E)$ [42]. For instance, writing

the grand potential as an integral involving $N(E)$, and using equation (5), gives the expression for the Weiss fields [21]

$$\vec{h}_{i\alpha} = -\frac{1}{\pi}\mathrm{Im}\int \mathrm{d}E f_{\mathrm{FD}}(E, T_{\mathrm{el}})\left(\frac{3}{4\pi}\int \mathrm{d}\vec{\hat{e}}_i\ \vec{\hat{e}}_i\ \ln\det \underline{D_{i\alpha}}^{-1}(\vec{\hat{e}}_i, E)\right) \tag{14}$$

where it is now necessary to write explicitly the energy dependence of $\underline{D_{i\alpha}}$ from equation (9). f_{FD} is the Fermi–Dirac distribution and we have distinguished the electronic temperature T_{el} from the 'magnetic' temperature T, discussed more in section 3.2.

2.7. Calculating the magnetocrystalline anisotropy

The MCA quantifies the change in (free) energy as a result of rotating the magnetization. In MARMOT we take $\mathcal{F}$ as our best estimate of the free energy, and focus on calculating the torque-like quantities $\partial\mathcal{F}/\partial\Theta$ and $\partial\mathcal{F}/\partial\varphi$. Here Θ and φ are the angles representing the global magnetization direction. The DLM formalism allows the resolution of the total torque into contributions from different sites and atom types, for instance

$$\partial\mathcal{F}/\partial\Theta = \sum_{i\alpha} c_{i\alpha}\partial\mathcal{F}/\partial\Theta_{i\alpha} \tag{15}$$

where now $\Theta_{i\alpha}$ refers to the magnetization of that particular atom type; explicitly, $\vec{\lambda}_{i\alpha} = \lambda_{i\alpha}\vec{\hat{n}}_{i\alpha} = \lambda_{i\alpha}(\sin\Theta_{i\alpha}\cos\varphi_{i\alpha}, \sin\Theta_{i\alpha}\sin\varphi_{i\alpha}, \cos\Theta_{i\alpha})$. It is convenient to consider the auxiliary quantity $\partial\mathcal{F}/\partial\vec{\hat{n}}_{i\alpha}$, given by [35]:

$$\frac{\partial\mathcal{F}}{\partial\vec{\hat{n}}_{i\alpha}} = -\frac{1}{\pi}\mathrm{Im}\int \mathrm{d}E f_{\mathrm{FD}}(E, T_{\mathrm{el}})\left(\int \mathrm{d}\vec{\hat{e}}_{i\alpha}\frac{\partial P_{0i\alpha}(\vec{\hat{e}}_{i\alpha})}{\partial\vec{\hat{n}}_{i\alpha}}[-\ln\det \underline{D_i}^{-1}(\vec{\hat{e}}_i, E)]\right). \tag{16}$$

The quantity $\partial P_{0i\alpha}(\vec{\hat{e}}_{i\alpha})/\partial\vec{\hat{n}}_{i\alpha}$ straightforwardly evaluates to $\lambda_{i\alpha}P_{0i\alpha}(\vec{\hat{e}}_{i\alpha})[\vec{\hat{e}}_{i\alpha} - \langle\vec{\hat{e}}_{i\alpha}\rangle]$, so $\partial\mathcal{F}/\partial\vec{\hat{n}}_{i\alpha}$ can be evaluated at the same cost as the Weiss fields. The angular derivatives are then obtained through the chain rule:

$$\begin{aligned}
\frac{\partial\mathcal{F}}{\partial\Theta_{i\alpha}} &= \frac{\partial\mathcal{F}}{\partial n_{i\alpha x}}\cos\Theta_{i\alpha}\cos\varphi_{i\alpha} + \frac{\partial\mathcal{F}}{\partial n_{i\alpha y}}\cos\Theta_{i\alpha}\sin\varphi_{i\alpha} - \frac{\partial\mathcal{F}}{\partial n_{i\alpha z}}\sin\Theta_{i\alpha}\\
\frac{\partial\mathcal{F}}{\partial\varphi_{i\alpha}} &= -\frac{\partial\mathcal{F}}{\partial n_{i\alpha x}}\sin\Theta_{i\alpha}\sin\varphi_{i\alpha} + \frac{\partial\mathcal{F}}{\partial n_{i\alpha y}}\sin\Theta_{i\alpha}\cos\varphi_{i\alpha}
\end{aligned} \tag{17}$$

The MCA constants can be inferred by calculating these angular derivatives for different magnetization angles. Taking the example of a uniaxial ferromagnet with anisotropy constant K_1, the angular dependence of $\mathcal{F}$ is $K_1\sin^2\Theta$. Therefore, $\partial F/\partial\Theta = K_1\sin 2\Theta$, so evaluating the derivative at $\Theta = 45^\circ$ yields K_1. Performing calculations for a number of different angles allows higher-order constants to be extracted.

2.8. Solving the single-site problem

The fundamental input to a MARMOT calculation is a set of spherically-symmetric, atom-centred potentials $\{V^{\sigma}_{i\alpha}(r)\}$, where σ labels the spin. $\{V^{\sigma}_{i\alpha}(r)\}$ will have been calculated within scalar-relativistic DFT, possibly using the CPA for compositional disorder, for a relatively simple spin reference state; either ordered ferro/antiferro/ferri-magnetic, or the fully disordered paramagnetic state. The spherical symmetry is enforced either by the muffin tin (MT) or atomic sphere (ASA) approximations. MARMOT takes these potentials and feeds them into a Schrödinger or four-component Dirac radial equation, depending on whether a non-, scalar- or fully-relativistic solution is required.

For the non- or scalar-relativistic case, the equations are constructed for each (l, σ) pair and solved to find $Z^{l\sigma}_{i\alpha}(r, E)$ and $J^{l\sigma}_{i\alpha}(r, E)$, which are regular or irregular at the origin, respectively. The equations are solved using a four-point predictor-corrector method using Calogero's approach, which expresses the solutions as superpositions of Riccati–Bessel functions [45]. The t-matrix elements $t_{i\alpha L}(\vec{\hat{z}}, E)$ are extracted from the value of the regular solution at the radius of the potential. The t-matrix is diagonal and degenerate in m for a given (l, σ).

As well as t-matrices, MARMOT calculates 'p-matrices' defined as follows:

$$\begin{aligned}
p^{zz}_{i\alpha L}(\vec{\hat{z}}, E) &= \int \mathrm{d}r\ r^2 Z^{l\sigma}_{i\alpha}(r, E)Z^{l\sigma}_{i\alpha}(r, E)\\
p^{s,zz}_{i\alpha L}(\vec{\hat{z}}, E) &= \pm\mu_{\mathrm{B}}\int \mathrm{d}r\ r^2 Z^{l\sigma}_{i\alpha}(r, E)Z^{l\sigma}_{i\alpha}(r, E)\\
p^{o,zz}_{i\alpha L}(\vec{\hat{z}}, E) &= m\ \mu_{\mathrm{B}}\int \mathrm{d}r\ r^2 Z^{l\sigma}_{i\alpha}(r, E)Z^{l\sigma}_{i\alpha}(r, E).
\end{aligned} \tag{18}$$

μ_B is the Bohr magneton, and the $\pm$ applies to spin up or down. There are also p^{zj} matrices, which are obtained by replacing the second Z in the integral with J, e.g. $p^{zj}_{i\alpha L}(\vec{\hat{z}}, E) = \int \mathrm{d}r\ r^2 Z^{l\sigma}_{i\alpha}(r, E) J^{l\sigma}_{i\alpha}(r, E)$. These matrices correspond to the different contributions to the Green's function in multiple-scattering theory [41], and are used to construct densities and magnetic moments integrated over space.

For the relativistic case, it is necessary to consider the combined spin-angular momentum quantum numbers (κ, m_j) instead of L. Each (κ, m_j) channel will have at least one regular and one irregular solution, $\Psi^{\kappa m_j}_{i\alpha}(\vec{r}, E)$ and $\Lambda^{\kappa m_j}_{i\alpha}(\vec{r}, E)$, respectively, which are four-component functions. Furthermore, the majority of channels are coupled to a second pair of solutions $\Psi^{\kappa' m_j}_{i\alpha}(\vec{r}, E)$ and $\Lambda^{\kappa' m_j}_{i\alpha}(\vec{r}, E)$, where $\kappa' = -\kappa - 1$. We find these solutions and the corresponding t-matrix elements $t^{m_j}_{i\alpha\kappa\kappa'}(\vec{\hat{z}}, E)$ using the same predictor-corrector and Calogero approach within the framework of reference [33], if necessary including the self-interaction correction or OPC as described in reference [39]. The Clebsch–Gordan coefficients are used to transform the t-matrix back into the L representation, to give $t_{i\alpha LL'}(\vec{\hat{z}}, E)$, which in general is non-diagonal and m-dependent [34].

The p-matrices are also formed in the (κ, m_j) representation and rotated. Focusing on the p^{zz} matrices, we have

$$
\begin{aligned}
p^{zz,m_j}_{i\alpha\kappa\kappa'}(\vec{\hat{z}}, E) &= \int \mathrm{d}\vec{r}\ \Psi^{\kappa m_j}_{i\alpha}(\vec{r}, E) \Psi^{\kappa' m_j \times}_{i\alpha}(\vec{r}, E) \\
p^{s,zz,m_j}_{i\alpha\kappa\kappa'}(\vec{\hat{z}}, E) &= \mu_B \int \mathrm{d}\vec{r}\ \Psi^{\kappa m_j}_{i\alpha}(\vec{r}, E) \tilde{\beta}\tilde{\sigma}_z \Psi^{\kappa' m_j \times}_{i\alpha}(\vec{r}, E) \\
p^{o,zz,m_j}_{i\alpha\kappa\kappa'}(\vec{\hat{z}}, E) &= \mu_B \int \mathrm{d}\vec{r}\ \Psi^{\kappa m_j}_{i\alpha}(\vec{r}, E) \tilde{\beta}\tilde{l}_z \Psi^{\kappa' m_j \times}_{i\alpha}(\vec{r}, E)
\end{aligned}
\tag{19}
$$

where $^\times$ refers to a left-hand solution [46], and $\tilde{\beta}\tilde{\sigma}_z$ and $\tilde{\beta}\tilde{l}_z$ are the relativistic spin and orbital momentum operators. The p^{zj} matrices are formed by replacing $\Psi^\times$ with $\Lambda^\times$.

Once the t and p matrices have been calculated, MARMOT makes no further distinction between relativistic and non-relativistic calculations. For instance, the structure constants are always calculated using a non-relativistic expression. Relativistic effects, like anisotropy or nonzero orbital moments, arise solely from the nondiagonal elements and broken orbital degeneracy of the t and p-matrices.

2.9. Calculating the integrated density, spin and orbital moments

The scattering path operator gives access to the electron Green's function and its associated properties. Taking traces over the relevant matrices gives an individual atom's contribution to the density, spin and orbital moments. The expressions for the three quantities have the same form, taking the density as an example:

$$
\rho_{i\alpha} = -\frac{1}{\pi}\mathrm{Im} \int \mathrm{d}E f_{\mathrm{FD}}(E, T_{\mathrm{el}})\ \mathrm{Tr} \int \mathrm{d}\vec{\hat{e}}_{i\alpha} P_{0i\alpha}(\vec{\hat{e}}_{i\alpha}) \left[\underline{p^{zz}_{i\alpha}}(\vec{\hat{e}}_{i\alpha}, E)\ \underline{\tau_{c,ii}}(E)\ \underline{D_{i\alpha}}(\vec{\hat{e}}_{i\alpha}, E) - \underline{p^{zj}_{i\alpha}}(\vec{\hat{e}}_{i\alpha}, E) \right]. \tag{20}
$$

The expressions for the spin $\mu^s_{i\alpha}$ and orbital $\mu^o_{i\alpha}$ moments replace $(\underline{p^{zz}_{i\alpha}}, \underline{p^{zj}_{i\alpha}})$ with $(\underline{p^{s,zz}_{i\alpha}}, \underline{p^{s,zj}_{i\alpha}})$ or $(\underline{p^{o,zz}_{i\alpha}}, \underline{p^{o,zj}_{i\alpha}})$, respectively. The temperature-dependent magnetization $\vec{M}(T)$ is formed as

$$
\vec{M}(T) = \sum_{i\alpha} c_{i\alpha} \vec{m}_{i\alpha} \left(\mu^s_{i\alpha} + \mu^o_{i\alpha} \right) \tag{21}
$$

which can straightforwardly be partitioned into spin and orbital contributions. The integrated density N is given by $N = \sum_{i\alpha} c_{i\alpha} \rho_{i\alpha}$.

The formulae for the Weiss fields and torques are derived from Lloyd's formula for the integrated density-of-states, which shows faster angular momentum convergence than expressions like equation (20) which are based on the Green's function. Therefore, the Weiss fields and torques are in general expected to be more numerically robust than the density, spin and orbital moments.

MARMOT can also calculate a spin-density-of-states, using the expression

$$
\rho^S_{i\alpha}(E) = \mathrm{Tr} \left\{ (\vec{n}_{i\alpha} \cdot \vec{S}) \left(-\frac{1}{\pi} \right) \mathrm{Im} \int \mathrm{d}\vec{\hat{e}}_{i\alpha} P_{0i\alpha}(\vec{\hat{e}}_{i\alpha}) \left[\underline{p^{zz}_{i\alpha}}(\vec{\hat{e}}_{i\alpha}, E)\ \underline{\tau_{c,ii}}(E)\ \underline{D_{i\alpha}}(\vec{\hat{e}}_{i\alpha}, E) - \underline{p^{zj}_{i\alpha}}(\vec{\hat{e}}_{i\alpha}, E) \right] \right\} \tag{22}
$$

Here, $\vec{S}$ is the spin operator. The value of this quantity at the Fermi level ($E = E_F$) is of particular interest when investigating magnetoresistive devices [30].

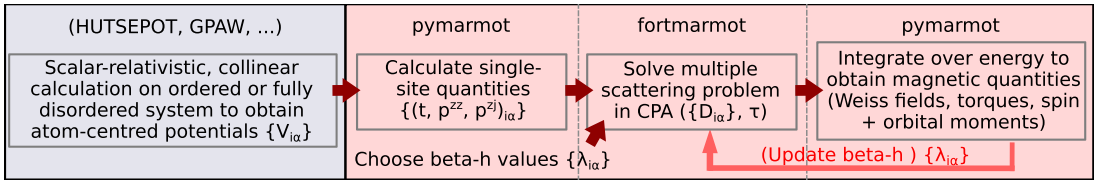

Figure 2. Schematic representation of a DLM calculation with MARMOT. The blue shading corresponds to the external potential calculation. The MARMOT calculation has been split into Python and FORTRAN parts for illustration, although the user is only required to interact with the Python-based pymarmot frontend.

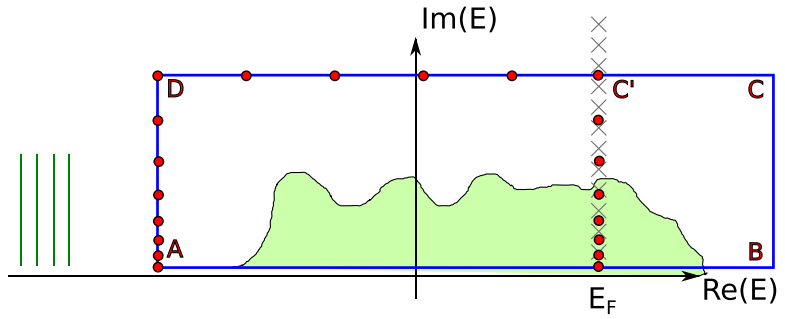

Figure 3. Representation of the energy contour used by MARMOT. The red circles show the complex energies at which the CPA equations are solved. The grey crosses are Matsubara frequencies. Note that the contribution to the integral from C'–C is obtained by extrapolation. The density-of-states of core and valence electrons is represented in green.

3. Technical details

3.1. Hybrid Python/FORTRAN workflow

Figure 2 demonstrates the steps of a typical calculation. The single-site potentials $\{V^{\sigma}_{i\alpha}(r)\}$ are obtained externally, usually with the HUTSEPOT DFT-KKR code [47], although as discussed in section 4.4 we have also used the projector-augmented wave DFT code GPAW [48]. The single-site scattering problem is then solved, to the relativistic level (full/scalar/non) specified by the user. The resulting single-site matrices are taken as input to solve the CPA problem at different energies. Finally, the energy integrals are performed to obtain the Weiss fields, and other quantities of interest.

Apart from the single-site potentials and the crystal structure, the user is required to specify the beta-h magnitude $\lambda_{i\alpha}$ and direction $\hat{\vec{n}}_{i\alpha}$ for each magnetic atom. If there is more than one magnetic sublattice, and self-consistency in the Weiss fields is desired (section 3.6), multiple CPA runs may be required (shown as the red arrow in figure 2).

Figure 2 also demonstrates how the calculation is partitioned between Python and FORTRAN code, referred to as pymarmot and fortmarmot. pymarmot is the frontend where the user sets up and analyses the calculation, with tools to solve the single-site problem and perform the post-CPA analysis including the energy integrations. fortmarmot is driven by pymarmot and concentrates solely on solving the CPA problem for a given set of t-matrices, crystal structure, energies and beta-h values. This hybrid approach allows us to exploit the speed and efficiency of FORTRAN for the most computationally-expensive parts of the calculation, whilst keeping the intuitive features of Python for the user interface and post-processing.

3.2. Energy integration

To calculate quantities like the Weiss fields (equation (14)), it is necessary to perform an energy integral of the form $-1/\pi\,\mathrm{Im}\int \mathrm{d}E f_{\mathrm{FD}}(E, T_{\mathrm{el}})F(E)$. This integral is evaluated as a contour, as shown in figure 3, which also sketches the density-of-states. The desired integral (A–B) is replaced with the integral along the two remaining nonzero legs of the contour (A–D–C) plus a sum over the Matsubara frequencies contained in the contour. MARMOT samples energies logarithmically along A–D and C'–E_{F}, and linearly along D–C', then uses spline interpolation between these points. The closest approach to the real axis is set by the first Matsubara frequency, $i\pi k_{\mathrm{B}}T_{\mathrm{el}}$, and the Fermi energy is chosen so that the integrated density (section 2.9) is equal to the expected number of electrons. The user controls how finely the energy is sampled (npdec, detop), the position of the top leg of the contour (eimax) and also must specify the energy of point A (ebot), which lies between the core and valence states as indicated in figure 3.

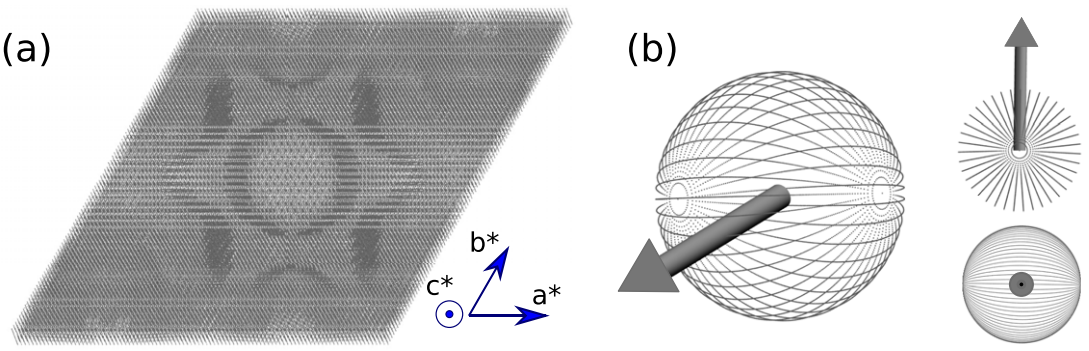

Figure 4. (a) A plan view of the reciprocal space unit cell, with $\vec{k}$-vectors used in the evaluation of τ shown as dots. Darker regions correspond to denser $\vec{k}$-point sampling. The structure in different *ab* planes appears as a projection. (b) The sampling scheme used to evaluate angular integrals. The grey arrow corresponds to the direction of $\vec{n}$, and each point corresponds to a (θ, ϕ) sample of the integral.

We made the distinction above between the electronic temperature $T_{\rm el}$, which enters the Fermi–Dirac function, and the 'magnetic' temperature T, which appears in the probability distribution as $\beta = 1/(k_{\rm B}T)$. In principle, this difference is artificial, and the same temperature should be used for both. However, the Weiss fields and torques are much less sensitive to $T_{\rm el}$ than T. Reducing the electronic temperature brings the Matsubara frequencies closer to the real axis, which increases the structure of the integrand and makes the Brillouin zone (BZ) integral more difficult to converge. The pragmatic solution is to fix $T_{\rm el}$ (e.g. 300 K), and only vary T. However, lower values of $T_{\rm el}$ should be investigated if very high precision is desired.

3.3. Brillouin zone integration

Calculating the scattering path operator with equation (7) requires integrating over the first BZ. To perform this integral, we use the adaptive sampling algorithm described in reference [49], which is designed to concentrate the BZ sampling in regions where the integrand has the most structure. The accuracy of the algorithm is controlled through a single parameter `tolint`, which is used to compare the evaluation of the trace of τ by Simpson's rule and the trapezoidal rule [49]. Since we generally investigate magnetic configurations with a low symmetry, the integral is performed across the full BZ.

Figure 4(a) demonstrates the algorithm in practice, by representing the k-vectors used to calculate τ at a hexagonal site (the Y atom in YCo_5) as points. An increased density of $\vec{k}$-points appears as a darker region in the picture. We see certain regions (which reflect the six-fold symmetry) where the $\vec{k}$-point density is very high. However, these regions correspond to a rather small fraction of the BZ overall. It would be very inefficient to achieve the same level of precision by sampling the entire BZ at this high $\vec{k}$-point density.

The methods of reference [49] are also used in the calculation of the structure constants. Specifically, `MARMOT` determines the two energy-dependent parameters η and x which give the optimum partitioning of real and reciprocal space for the Ewald evaluation of $\underline{\underline{G_0}}(E, \vec{k})$. The efficiency of the structure constants calculation is increased by pre-computing the parts of the sum which are independent of $\vec{k}$.

3.4. Angular integration

The equations used in the CPA, Weiss fields and torques all involve integrals over the unit sphere, $\int \mathrm{d}\vec{\hat{e}}_i F(\vec{\hat{e}}_i)$. These are carried out by sampling the directions linearly in $\sin\theta_i$ and ϕ_i. For the θ_i integral, we rotate the unit sphere so that the poles ($\theta_i = 0, \pi$) are perpendicular to $\vec{\hat{n}}_i$. This rotation is shown in figure 4(b) and ensures that the angular integral has the highest sampling in the region where $P(\vec{\hat{e}}_i)$ is largest and has the most structure. The user controls the density of the angular grids through the parameters `ntheta` and `nphi`.

3.5. Parallelism

At present, `MARMOT` exploits the trivial parallelism over energy for the CPA problem. `pymarmot` also parallelizes the single-site scattering over the sites and atomic types, making use of the `multiprocessing` package. Although parallelizing over energy is theoretically highly efficient, there is a problem of load balance: the integrand becomes progressively more structured along the A–B–C'–$E_{\rm F}$ path of figure 3. As a result, processors working on the final energy points require much more time than others due to the increased number of $\vec{k}$-vectors required to converge the integral. In future, we intend to implement additional levels of CPA parallelization, e.g. over the BZ volume and/or sublattice sites.

3.6. Self-consistency in Weiss fields and parameterizing the grand potential

In the discussion surrounding equation (5), we noted that there should be a self-consistency between the Weiss fields and the probability distribution used to calculate them. Considering an input beta-h value λ^X and output Weiss field h^X_{out}, and recalling $\beta = 1/(k_B T)$, the self-consistent solution at a temperature T must satisfy

$$\frac{\lambda^X}{h^X_{\text{out}}} = \frac{\lambda^Y}{h^Y_{\text{out}}} = \frac{\lambda^Z}{h^Z_{\text{out}}} = \ldots = \frac{1}{k_B T}, \tag{23}$$

where X, Y, Z, … refer to different magnetic sublattices. This condition is equivalently expressed by defining magnetic sublattice temperatures $T_X = h^X_{\text{out}}/(k_B \lambda^X)$ and demanding that all sublattices have the same temperature T. Iterative strategies to determine the set of self-consistent beta-h values are discussed in section 4.3.

As an alternative to finding the self-consistent probability distribution, MARMOT can be used to parameterize the grand potential in terms of magnetic order parameters. In this approach, we replace the thermally-averaged grand potential $\langle\Omega\rangle_{0,T}$ with a model expression which is a differentiable function of the order parameters [28]. The differential form of equation (5) then yields parameterizations of the Weiss fields which can be fitted to the output from MARMOT. For instance, for a simple magnetic system with a single order parameter m we might consider a Landau-type expression:

$$\langle\Omega\rangle_{0,T} = -\frac{1}{2} J_0 m^2 - \frac{1}{4} J_1 m^4 + \cdots, \tag{24}$$

where J_0 and J_1 are coefficients to be determined. Differentiating equation (24) gives $h = (J_0 m + J_1 m^3 + \cdots)$. Performing a set of MARMOT calculations for different input beta-h values (corresponding to different m, through equation (3)) allows J_0 and J_1 to be determined through a least-squares fitting. Such an approach provides insight into the fundamental nature of the magnetic interactions (quadratic, biquadratic etc) and allows the magnetic phase diagram to be mapped out, possibly discovering new minima of the magnetic free energy [9, 22, 25, 26, 28].

4. Examples

4.1. Computational details

In this section we show some practical calculations performed with MARMOT. All angular momentum expansions were performed up to and including the f angular momentum channel, i.e. $l_{\max} = 3$. Exchange and correlation was modelled within the local-spin-density approximation (LSDA) as parameterized by Vosko *et al* [50]. The angular sampling of the CPA integral and the tolerance for the BZ integration were set at their MARMOT default values of 240×40 and 10^{-5}, respectively, and the electronic temperature in the Fermi–Dirac function was set to 300 K. Other details specific to the different calculations are given as appropriate.

4.2. bcc Fe

We first demonstrate MARMOT's application to the canonical example of a ferromagnet, bcc Fe. We use the LSDA-optimized lattice constant of $5.20 a_0$ (where a_0 is the Bohr radius) and perform the initial self-consistent, scalar-relativistic calculation using the HUTSEPOT code [47]. This initial calculation is performed for paramagnetic state, using the MT approximation for the potential. In the CPA, this state ($\lambda = 0$) can be modelled equivalently as a 50:50 mix of collinear spin up and down atoms at each site [21]. This HUTSEPOT calculation yields local moments of 1.75 μ_B for the Fe atoms.

We then take the generated potentials and perform a set of finite temperature calculations with MARMOT, remaining in the scalar-relativistic approximation. For a set of λ values between 0.05–30, we calculated the Weiss field h experienced by the Fe atoms. The results are shown in the left panel of figure 5, where we use equation (3) to relate λ to the order parameter m. In the right panel of figure 5, we plot the magnetization (equation (21)) against the temperature, obtained from h as $T = h/(k_B \lambda)$.

It can be seen that for $m < 0.4$ the Weiss field is linear in order parameter, i.e. $h = J_0 m$, while an additional m^3 term is required to fit the data across the full range of m. Using the expansion of equation (24) up to m^4, we find values of 332 and -78 meV for J_0 and J_1, which can be related to the Curie temperature T_C as follows: in the small m limit, equation (3) reduces to $m \to \lambda/3$, with the temperature at which m vanishes corresponding to T_C. Since $\lambda = \beta h$, we have $m = \frac{h}{J_0} = \frac{h}{3 k_B T_C}$, or

$$T_C = \frac{J_0}{3 k_B}. \tag{25}$$

Accordingly, we calculate a Curie temperature of 1283 K, to be compared to the experimental value of 1040 K [51].

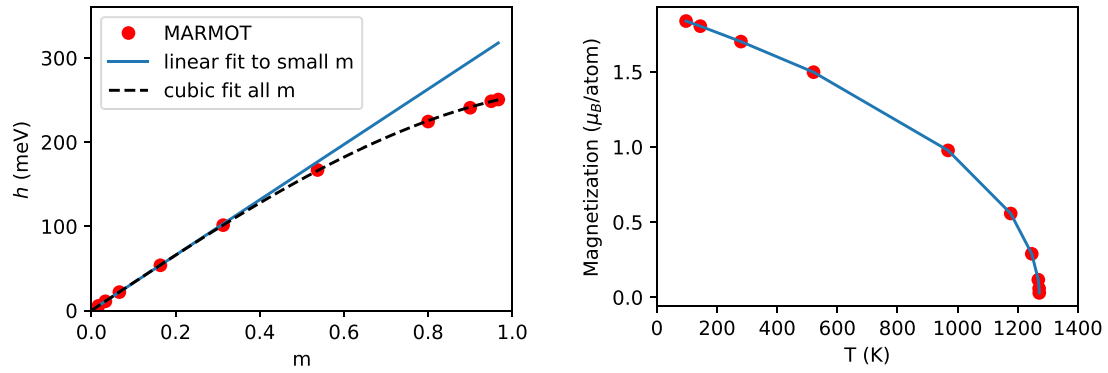

Figure 5. MARMOT calculations for bcc Fe, shown as red circles, of the Weiss field as a function of order parameter (left) and magnetization as a function of temperature (right).

The procedure above may be applied exactly to any system comprising a single magnetic sublattice. Specific to bcc Fe, we point out three important facts: first, the range of order parameters where a quadratic expansion of the energy is valid, $m < 0.4$, corresponds to rather high temperatures, $T > 1000$ K. To explain the behaviour of the Weiss fields at lower temperatures, including room temperature, the quartic contribution J_1 must also be included. Second, our initial scf calculation was performed for the paramagnetic (PM) reference state. Using the ferromagnetic reference state instead gives a much larger T_C, 1785 K, which shows that the material is deviating from local moment behaviour. Finally, the value of T_C is also sensitive to the lattice parameter; recomputing T_C using the PM reference state at a lattice constant of $5.47a_0$ (measured experimentally at the Curie temperature [52]) gives a value of 1951 K.

4.3. Laves phase $GdFe_2$

Next we consider a ferrimagnet, $GdFe_2$. The RFe_2 family of magnets (R = rare earth) crystallized in the cubic Laves phase are remarkable for their giant magnetostriction, particularly the Tb–Dy alloy Terfenol-D [53]. As is usually the case with such magnets [54], there is an antiferromagnetic coupling between the spin moments of the rare earth and the transition metal atoms, so that resultant magnetization is the difference of the moments associated with the Gd and Fe sublattices. Taking approximate moments of 7 and 2 μ_B for Gd and Fe respectively, we therefore expect the total magnetization of $\sim$3 μ_B to point in the same direction as the Gd spins. This behaviour is different to other famous magnets in this class, e.g. $Gd_2Fe_{14}B$, Gd_2Co_{17} or $GdCo_5$, where the higher transition metal content leads to the total magnetization pointing in the opposite direction to the Gd spins [39].

To generate the atom-centred potentials, we perform scalar-relativistic calculations with HUTSEPOT at a fixed lattice constant of 7.405 Å, corresponding to the experimentally-measured room temperature value [55]. Since the Gd-4*f* electrons are not well described within the LSDA, we apply the LSIC to this spin subshell [36]. The potential is described in the ASA with Wigner–Seitz radii of 3.15 and $2.94a_0$ for Gd and Fe, respectively. We use the zero temperature, ferrimagnetic configuration as our reference state, and calculate moments of 7.67 and 2.11 μ_B for the Gd and Fe atoms, giving a total magnetization of 3.45 μ_B/FU.

We next use MARMOT to perform finite temperature, fully-relativistic calculations. We take the magnetization to be aligned along the [001] direction, which results in there being two distinct λ values, one for Gd and one for Fe. The self-consistency condition (equation (23)) takes the form

$$\frac{\lambda^{\mathrm{Gd}}}{h^{\mathrm{Gd}}_{\mathrm{out}}} = \frac{\lambda^{\mathrm{Fe}}}{h^{\mathrm{Fe}}_{\mathrm{out}}} = \frac{1}{k_{\mathrm{B}}T} \tag{26}$$

We generally choose between two iteration schemes to determine the self-consistent λ values: 'fixed-T' and 'fixed-λ' [56]. In the first case, λ values are updated as

$$\lambda^{\mathrm{X}}_{\mathrm{next}} = \frac{h^{\mathrm{X}}_{\mathrm{out}}}{k_B T}. \tag{27}$$

This scheme is useful where one is interested in particular temperatures well below T_C. Close to T_C, however, the 'fixed-T' scheme takes many steps to reach convergence and it is more efficient to fix λ on one sublattice Y to a small value, and update the other λ values as

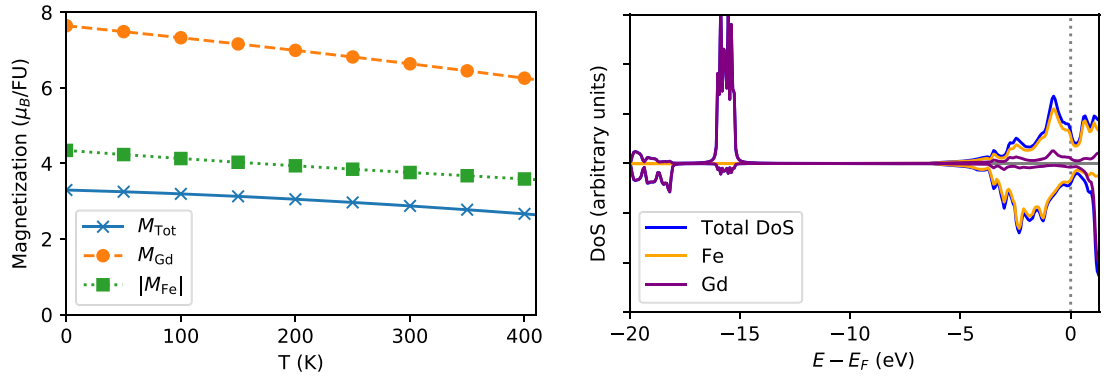

Figure 6. MARMOT calculations for $GdFe_2$, showing the temperature-dependent total and sublattice-resolved magnetization (left) and the finite-temperature, spin-resolved density-of-states (right), which shows clearly the Gd-4*f* electrons.

$$\lambda^{\mathrm{X}}_{\mathrm{next}} = \lambda^{\mathrm{Y}} \frac{h^{\mathrm{X}}_{\mathrm{out}}}{h^{\mathrm{Y}}_{\mathrm{out}}}. \tag{28}$$

MARMOT has built-in functions to automate the self-consistency procedure.

In figure 6, we show the magnetization vs temperature curve calculated for $GdFe_2$ using the (fixed-T) iterative method, up to a temperature of 400 K. The figure also shows the decomposition of the magnetization into the contributions from the Gd and Fe sublattices. The magnetization includes the orbital contribution to the moments, but it is relatively small; at $T = 0$ K, the orbital moment calculated for each Fe atom is 0.04 μ_{B}, while for Gd it is an order of magnitude smaller. The magnetization at 300 K is 2.88 μ_{B}/FU, a reduction of 0.42 μ_{B}/FU from its zero temperature value of 3.30 μ_{B}/FU. These values compare quite well to the experimental measurements of 3.35 and 2.71 μ_{B}/FU at 4 and 300 K, reported in reference [57], although we note the calculated magnetization decays more slowly with temperature. To investigate this decay further and obtain T_{C}, we generalize the small-m expansion of the grand potential (equation (24)) to multiple magnetic sublattices, keeping only quadratic terms:

$$\langle \Omega \rangle_{0,T} \approx -\frac{1}{2} \sum_{\mathrm{X,Y}} J_{\mathrm{XY}} m_{\mathrm{X}} m_{\mathrm{Y}} \tag{29}$$

Here, X and Y label magnetic sublattices, and in general have multiple atoms within the unit cell associated with them, quantified by the multiplicity N_X; for Laves-phase $GdFe_2$ magnetized along [001], $N_{\mathrm{Gd}} = 2$ and $N_{\mathrm{Fe}} = 4$. Furthermore, $J_{XY} = J_{YX}$. The Weiss field on a particular atom i, which forms part of sublattice X, is given by

$$h_i = \frac{1}{N_{\mathrm{X}}} \sum_{Y} J_{\mathrm{XY}} m_{\mathrm{Y}} \tag{30}$$

where the sum is over all sublattices (including X), and the multiplicity factor arises because $h_i = -\partial \langle \Omega \rangle_{0,T} / \partial m_i = (\partial \langle \Omega \rangle_{0,T} / \partial m_{\mathrm{X}}) \times (\partial m_X / \partial m_i)$. It is convenient to use equation (30) to introduce a matrix with elements $\mathcal{M}_{\mathrm{XY}} = J_{\mathrm{XY}} / N_{\mathrm{X}}$; for $GdFe^2$ $\mathcal{M}$ is a 2×2 matrix. Introducing $\vec{H} = (h^{\mathrm{Gd}}, h^{\mathrm{Fe}})$ and taking the small m limit yields the eigenvalue equation

$$\frac{1}{3k_{\mathrm{B}}T_{\mathrm{C}}} \mathcal{M}\, \vec{H} = \vec{H} \tag{31}$$

which shows how T_{C} is given by the largest eigenvalue of the matrix formed as $\mathcal{M}/(3k_{\mathrm{B}})$.

The J_{XY} coefficients can be obtained from least squares fitting of Weiss fields calculated for various combinations of small λ values. For $GdFe_2$ we perform six calculations, using combinations of λ_{Gd} and λ_{Fe} with values of 0.00, 0.05 or 0.10. These small values of λ ensure we remain in the regime where the Weiss fields are linear in m and above numerical noise. The extracted values of the J_{XY} parameters are $J_{\mathrm{Gd-Gd}} = 99.2$, $J_{\mathrm{Gd-Fe}} = 417.6$ and $J_{\mathrm{Fe-Fe}} = 1042.6$ meV, which combine to give a T_{C} of 1302 K. This is an overestimate compared to the experimentally measured Curie temperature of 790 K [57]. Referring to the previous calculations on bcc Fe we note that we are using a FM reference state and experimental lattice constants, which both resulted in an increased T_{C} compared to experiment.

In addition to the magnetization, in figure 6 we show the spin-resolved density-of-states (DoS) calculated at $T = 300$ K, which corresponds to $(\lambda^{\mathrm{Gd}}, \lambda^{\mathrm{Fe}}) = (8.17, 7.65)$. The DoS around the Fermi energy E_{F} is composed predominantly of Fe-3*d* states, with a notable contribution from the Gd-5*d* state in the majority spin channel.

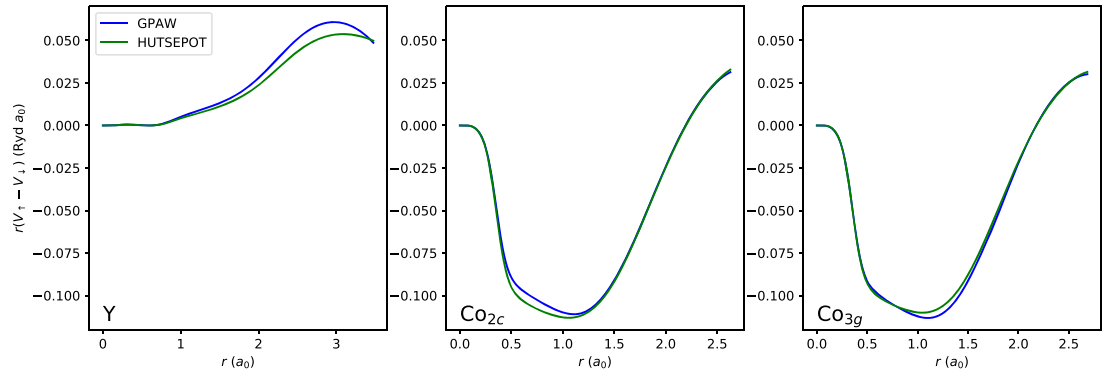

Figure 7. The difference in atom-centred, spherically-symmetric potentials for the spin-up and down channels for the three distinct atomic sites in the YCo_5 unit cell. The potentials were calculated for the zero-temperature, ferrimagnetic state using the GPAW and HUTSEPOT codes.

The LSIC places the Gd-4*f* states 15 eV below the Fermi level, and the Gd-5*p* semicore states are also evident at lower energy. The unoccupied Gd-4*f* states are visible in the minority spin channel, 1.5 eV above E_F. We note that the spin–orbit interaction mixes spin up and down states so that the Gd-4*f* peak at −15 eV has a contribution in the minority spin channel, as shown previously for the RCo_5 compounds [39].

4.4. YCo_5

For our final example we consider the hexagonal magnet YCo_5, and demonstrate the use of the GPAW code [48] to generate the initial potentials, as an alternative to HUTSEPOT. YCo_5 adopts the $CaCu_5$ structure (space group 191), and we use the values $a = 4.950$ and $c = 3.986$ Å for the lattice constants, as measured experimentally at 300 K [55]. For the GPAW calculation, we use a plane-wave expansion of the wavefunctions up to a maximum cutoff energy of 1200 eV, and sample the BZ on a $20 \times 20 \times 20$ grid, with a Fermi–Dirac smearing of 0.01 eV. We use the standard PAW datasets (v0.9.2) to account for the core-valence interaction. The calculated zero temperature, ferromagnetic state has a magnetization of 7.03 μ_B/FU. The magnetization can be decomposed into local moments of 1.50, 1.53 and −0.16 μ_B for Co_{2c}, Co_{3g} and *Y*, where 2*c* and 3*g* label the two crystallographically distinct Co sites.

For comparison, we consider the same system using HUTSEPOT, within the ASA. Here, the calculated magnetization is 7.19 μ_B/FU, with local moments of 1.53, 1.47 and −0.31 μ_B. Although both calculations solve the equations of DFT in the LSDA, there are a number of technical differences. HUTSEPOT employs a spherical approximation for the potential, while GPAW does not. But, HUTSEPOT treats the core electrons and their interactions with the valence explicitly, while GPAW freezes the core electrons and treats the valence interaction through a finite basis of projector functions [58]. Even the definition of local moments varies between implementations, with HUTSEPOT using the integrated magnetization in the WS spheres, compared to GPAW which projects onto local orbitals.

MARMOT requires the Kohn–Sham (KS) potential in a spherically-symmetric, atom-centred form on a radial grid, which is exactly the form used by HUTSEPOT. However, in GPAW, the KS potential consists of a smooth part (here represented in Fourier space) and atom-centred corrections. The post-processing procedure of reconstructing the 'all-electron' KS potential in atom-centred form, has been discussed previously in the context of calculating crystal field (CF) coefficients [59]. In CF theory, one is interested in the full angular expansion of the potential, but only the spherically-symmetric $l = m = 0$ components are required for the MARMOT calculation.

In figure 7 we show a comparison of the potentials obtained in GPAW and HUTSEPOT. Specifically, we consider the difference between the spin up and down components of the potential, which is proportional to the effective exchange–correlation magnetic field, for each crystallographically-distinct atom. The curves clearly follow the same shape and overlap in certain regions of space, but there are also observable differences. The differences have a quantitative effect on the calculated properties, as discussed below.

In addition to constructing the potentials as spherical averages, to perform a MARMOT calculation we also need to decide on the radii of the WS spheres. Within the ASA, the total volume of the spheres must equal the volume of the unit cell, but if there are multiple atoms in the cell then the ratios of the WS radii remain a free parameter. Here, we fix the radii to be 1.39, 1.42 and 1.84 Å for Co_{2c}, Co_{3g} and *Y*, which are values which have been used previously [60]. We discuss possible alternatives below.

Using these potentials, we perform a set of fully-relativistic MARMOT calculations for temperatures between 0–300 K. The magnetization at zero temperature is calculated to be 8.05 μ_B/FU. This consists of a spin contribution of 7.46 μ_B/FU, (which is larger by 0.4 μ_B/FU than the original scalar-relativistic GPAW calculation),

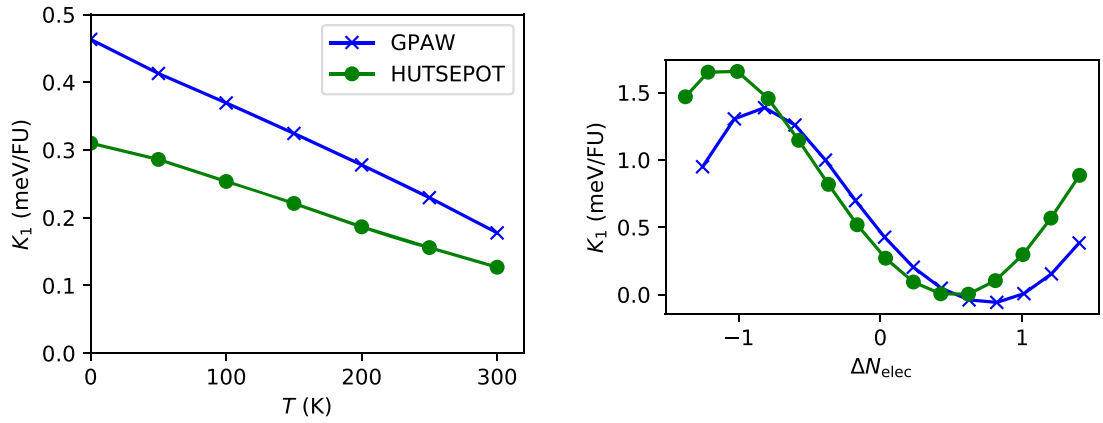

Figure 8. MARMOT calculations of the magnetocrystalline anisotropy constant K_1 as a function of temperature (left) or at zero temperature, as a function of electron number (right). The calculations were performed using potentials generated either with the GPAW or HUTSEPOT codes.

and an orbital contribution of 0.58 μ_B/FU, due to orbital moments of $\sim 0.1\mu_B$ on each Co atom. As well as obtaining the self-consistent λ values, we also calculate the MCA energy from the torque when the material is magnetized along the [101] direction [61]. This is plotted in figure 8, and reduces from a value of 0.46 meV/FU (0.88 MJ m^{-3}) at $T = 0$ K to 0.18 meV/FU (0.34 MJm^{-3}) at $T = 300$ K. Also, following the same procedure as for $GdFe_2$, we parameterize a small-m expansion to obtain T_C, and find a value of 864 K.

Now we repeat the MARMOT calculations starting from the HUTSEPOT potentials. The anisotropy energy is shown in figure 8, with values of 0.31 and 0.13 meV/FU at $T = 0$ and 300 K, respectively. The zero-T magnetization is 7.84 μ_B/FU (7.23 and 0.61 μ_B/FU spin and orbital contributions, respectively), and the calculated T_C is 874 K.

Experimentally, values between 7.9–8.4 μ_B/FU have been reported for the magnetization at 4 K [55, 62], and the anisotropy energy has been measured to be approximately 4 meV/FU [63, 64]. The underestimation of the anisotropy by the LSDA has been observed previously, and including an OPC both strengthens the anisotropy and increases the magnitudes of the orbital moments [65]. Applying the OPC here gives zero-T anisotropies of 6.4 meV/FU and 4.5 meV/FU, starting from the GPAW and HUTSEPOT calculations, respectively. Experimentally-measured values of T_C range from 940–1000 K [55, 64], i.e. larger than the current calculations by 100 K. Taking account of thermal expansion by using higher-temperature lattice parameters was found to increase T_C by 42 K in $GdCo_5$ [60].

These calculations on YCo_5 serve as a proof-of-concept demonstration of using GPAW's plane-wave implementation of collinear spin-DFT to generate potentials for a MARMOT calculation, which show qualitatively the same behaviour as potentials generated with the KKR in HUTSEPOT. The attraction of this approach is that it widens the accessibility of MARMOT, since GPAW and other similar codes have a large community of users and developers. However, more testing and development is required in order to understand better the limitations of the approach. Probably the most important factor is that MARMOT approximates the potential as spherically symmetric, either within the MT picture or the ASA. The fact that HUTSEPOT makes the same approximation means that this code is the sensible choice to calculate the self-consistent charge and potential: it allows us to start the MARMOT calculation from a variational minimum within the spherical approximation. By contrast, in the GPAW case we are starting from a spherically-symmetrized version of the self-consistent full potential, which is not a variational minimum.

An additional question is the choice of WS radii. The values used here were in fact originally derived from a GPAW calculation [60], which chose the set of radii which minimized the sum of the deviation of the potentials from their spherical average, subject to the single constraint that the sum of the WS sphere volumes equals the unit cell volume. A modification to this approach would be to include the additional constraint that the charge contained within the WS spheres integrates to the expected number of electrons in the unit cell. Having an accurate value for this number is expected to be particularly important when calculating the anisotropy, since this quantity is extremely sensitive to the Fermi level position [65], as shown in figure 8.

5. Conclusions and outlook

The DLM approach allows the inclusion of finite-temperature magnetic disorder within first-principles DFT calculations. The fundamentals of the DLM were set down in the 1980s [21], but continued developments

have allowed progressively more ambitious problems to be tackled [24–31]. MARMOT assimilates many of these developments into a single code base, retaining the fundamental speed and efficiency of FORTRAN for the most computationally-intensive part of the problem whilst providing a Python-based frontend to handle the user interface and post-processing of data.

The code structure implemented here will form the base for the next round of progress. Apart from a technical aspect (improved parallelization), we have already indicated one avenue for development, which is to interface MARMOT with a wider range of DFT packages for the initial generation of potentials. We have used GPAW as a proof-of-concept, and highlighted the question of how best to sphericize ('muffin-tinnize') the potentials. This question applies to any full-potential-type calculations, such as those using plane-waves and pseudopotentials like CASTEP or Quantum ESPRESSO [66, 67]. For codes capable of performing sphericized self-consistent calculations, such as QUESTAAL, sprKKR and juKKR [41, 68, 69], the task is more straightforward, requiring Python-based parsers to read in the different potential formats.

The Python frontend presents other opportunities for development. Interfacing with the atomic simulation environment (ASE) [70] would simplify the generation of crystal structures. Python also facilitates increased automation across the whole calculation, opening the prospect of high-throughput calculations as part of a larger workflow. For instance, for simple materials it is possible to determine an analytical form of the magnetic potential energy $\langle\Omega\rangle_{0,T}$ by hand, writing down and fitting expressions like equation (29). However, for materials with multiple magnetic sublattices and/or complicated exchange terms, an automated method of determining $\langle\Omega\rangle_{0,T}$ becomes essential.

We also note the important contribution that first-principles calculations can play in providing the input parameters for larger length- and timescale simulations, based on atomistic spin dynamics or micromagnetics [13, 71]. By finding the 'best' analytical expression for $\langle\Omega\rangle_{0,T}$ in MARMOT, we can specify the most appropriate form of the magnetic interactions which should enter the larger-scale models. Using MARMOT to obtain numerical values of the parameters required to describe these interactions will facilitate predictive modelling of magnetic materials across different length-scales.

Data availability statement

The MARMOT software package is available to the computational magnetism community to be used as a research tool. The software can be obtained by contacting the authors, or by visiting the website [72].

Acknowledgments

This work was carried out with the support of a Royal Society Research Grant RGS\R1\201151. We acknowledge and thank the many contributors and collaborators who have participated in the development of previous iterations of the DLM code.

ORCID iDs

Christopher E Patrick https://orcid.org/0000-0002-1843-1269
Julie B Staunton https://orcid.org/0000-0002-3578-8753

References

[1] Skjærvø S H, Marrows C H, Stamps R L and Heyderman L J 2020 *Nat. Rev. Phys.* **2** 13
[2] Takagi H, Takayama T, Jackeli G, Khaliullin G and Nagler S E 2019 *Nat. Rev. Phys.* **1** 264
[3] Hellman F *et al* 2017 *Rev. Mod. Phys.* **89** 025006
[4] Kitanovski A 2020 *Adv. Energy Mater.* **10** 1903741
[5] Vedmedenko E Y *et al* 2020 *J. Phys. D: Appl. Phys.* **53** 453001
[6] Gutfleisch O, Willard M A, Brück E, Chen C H, Sankar S G and Liu J P 2011 *Adv. Mater.* **23** 821
[7] Sanvito S *et al* 2017 *Sci. Adv.* **3** 1602241
[8] Grytsiuk S, Hoffmann M, Hanke J-P, Mavropoulos P, Mokrousov Y, Bihlmayer G and Blügel S 2019 *Phys. Rev.* B **100** 214406
[9] Boldrin D *et al* 2018 *Phys. Rev.* X **8** 041035
[10] Okamoto S *et al* 2019 *Acta Mater.* **178** 90
[11] Cao Y *et al* 2021 *Phys. Rev. Lett.* **127** 055501
[12] Nayak A K *et al* 2015 *Nat. Mater.* **14** 679
[13] Evans R F L 2018 Atomistic spin dynamics *Handbook of Materials Modeling: Applications: Current and Emerging Materials* ed W Andreoni and S Yip (Berlin: Springer), pp 1–23
[14] Kotliar G, Savrasov S Y, Haule K, Oudovenko V S, Parcollet O and Marianetti C A 2006 *Rev. Mod. Phys.* **78** 865
[15] Liechtenstein A I, Katsnelson M I, Antropov V P and Gubanov V A 1987 *J. Magn. Magn. Mater.* **67** 65
[16] Terasawa A, Matsumoto M, Ozaki T and Gohda Y 2019 *J. Phys. Soc. Japan* **88** 114706

[17] He X, Helbig N, Verstraete M J and Bousquet E 2021 *Comput. Phys. Commun.* **264** 107938
[18] Khmelevska T, Khmelevskyi S and Mohn P 2008 *J. Appl. Phys.* **103** 073911
[19] Ebert H, Mankovsky S, Chadova K, Polesya S, Minár J and Ködderitzsch D 2015 *Phys. Rev.* B **91** 165132
[20] Kudrnovský J, Drchal V, Turek I, Khmelevskyi S, Glasbrenner J K and Belashchenko K D 2012 *Phys. Rev.* B **86** 144423
[21] Györffy B L, Pindor A J, Staunton J, Stocks G M and Winter H 1985 *J. Phys. F: Met. Phys.* **15** 1337
[22] Mendive-Tapia E and Staunton J B 2017 *Phys. Rev. Lett.* **118** 197202
[23] Staunton J B, Ostanin S, Razee S S A, Gyorffy B L, Szunyogh L, Ginatempo B and Bruno E 2004 *Phys. Rev. Lett.* **93** 257204
[24] Hughes I D *et al* 2007 *Nature* **446** 650
[25] Staunton J B, Banerjee R, dos Santos Dias M, Deak A and Szunyogh L 2014 *Phys. Rev.* B **89** 054427
[26] Petit L, Paudyal D, Mudryk Y, Gschneidner K A, Pecharsky V K, Lüders M, Szotek Z, Banerjee R and Staunton J B 2015 *Phys. Rev. Lett.* **115** 207201
[27] Marchant G A, Patrick C E and Staunton J B 2019 *Phys. Rev.* B **99** 054415
[28] Mendive-Tapia E and Staunton J B 2019 *Phys. Rev.* B **99** 144424
[29] Patrick C E and Staunton J B 2019 *Phys. Rev. Mater.* **3** 101401
[30] Nawa K, Kurniawan I, Masuda K, Miura Y, Patrick C E and Staunton J B 2020 *Phys. Rev.* B **102** 054424
[31] Patrick C E, Marchant G A and Staunton J B 2020 *Phys. Rev. Appl.* **14** 014091
[32] Lejaeghere K *et al* 2016 *Science* **351** aad3000]]
[33] Strange P, Ebert H, Staunton J B and Gyorffy B L 1989 *J. Phys.: Condens. Matter.* **1** 2959
[34] Strange P 1998 *Relativistic Quantum Mechanics* (Cambridge: Cambridge University Press)
[35] Staunton J B, Szunyogh L, Buruzs A, Gyorffy B L, Ostanin S and Udvardi L 2006 *Phys. Rev.* B **74** 144411
[36] Lüders M, Ernst A, Däne M, Szotek Z, Svane A, Ködderitzsch D, Hergert W, Györffy B L and Temmerman W M 2005 *Phys. Rev.* B **71** 205109
[37] Eriksson O, Brooks M S S and Johansson B 1990 *Phys. Rev.* B **41** 7311
[38] Ebert H and Battocletti M 1996 *Solid State Commun.* **98** 785
[39] Patrick C E and Staunton J B 2018 *Phys. Rev.* B **97** 224415
[40] Györffy B L and Stocks G M 1979 First principles band theory for random metallic alloys *Electrons in Disordered Metals and at Metallic Surfaces* (*Nato Science Series B*) ed P Phariseau and B Györffy (Berlin: Springer) pp 89–192 ch 4
[41] Ebert H, Ködderitzsch D and Minár J 2011 *Rep. Prog. Phys.* **74** 096501
[42] Faulkner J S, Stocks G M and Wang Y 2018 *Multiple Scattering Theory* (Bristol: IOP Publishing)
[43] Peierls R 1938 *Phys. Rev.* **54** 918
[44] Deák A, Simon E, Balogh L, Szunyogh L, dos Santos Dias M and Staunton J B 2014 *Phys. Rev.* B **89** 224401
[45] Calogero F 1967 *Variable Phase Approach to Potential Scattering* (New York: Academic)
[46] Tamura E 1992 *Phys. Rev.* B **45** 3271
[47] Däne M, Lüders M, Ernst A, Ködderitzsch D, Temmerman W M, Szotek Z and Hergert W 2009 *J. Phys.: Condens. Matter.* **21** 045604
[48] Enkovaara J *et al* 2010 *J. Phys.: Condens. Matter.* **22** 253202
[49] Bruno E and Ginatempo B 1997 *Phys. Rev.* B **55** 12946
[50] Vosko S H, Wilk L and Nusair M 1980 *Can. J. Phys.* **58** 1200
[51] Tatsumoto E and Okamoto T 1959 *J. Phys. Soc. Japan* **14** 1588
[52] Basinski Z S, Hume-Rothery W and Sutton A L 1955 *Proc. R. Soc.* A **229** 459
[53] Clark A E 1980 Magnetostrictive rare earth-Fe_2 compounds *Handbook of Ferromagnetic Materials* vol 1 (Amsterdam: Elsevier) ch 7, p 531
[54] Brooks M S S, Eriksson O and Johansson B 1989 *J. Phys.: Condens. Matter.* **1** 5861
[55] Andreev A V 1995 Thermal expansion anomalies and spontaneous magnetostriction in rare-earth intermetallics with cobalt and iron *Handbook of Magnetic Materials* vol 8 (Amsterdam: Elsevier) ch 2, p 59
[56] Matsumoto M, Banerjee R and Staunton J B 2014 *Phys. Rev.* B **90** 054421
[57] Mansmann M and Wallace W E 1964 *J. Chem. Phys.* **40** 1167
[58] Blöchl P E 1994 *Phys. Rev.* B **50** 17953
[59] Patrick C E and Staunton J B 2019 *J. Phys.: Condens. Matter.* **31** 305901
[60] Patrick C E, Kumar S, Balakrishnan G, Edwards R S, Lees M R, Mendive-Tapia E, Petit L and Staunton J B 2017 *Phys. Rev. Mater.* **1** 024411
[61] Patrick C E, Kumar S, Balakrishnan G, Edwards R S, Lees M R, Petit L and Staunton J B 2018 *Phys. Rev. Lett.* **120** 097202
[62] Buschow K H J 1977 *Rep. Prog. Phys.* **40** 1179
[63] Alameda J M, Givord D, Lemaire R and Lu Q 1981 *J. Appl. Phys.* **52** 2079
[64] Yermolenko A S 1980 *Fiz. Metal. Metalloved.* **50** 741
[65] Daalderop G H O, Kelly P J and Schuurmans M F H 1996 *Phys. Rev.* B **53** 14415
[66] Clark S J, Segall M D, Pickard C J, Hasnip P J, Probert M I J, Refson K and Payne M C 2005 *Z. Kristallogr. Cryst. Mater.* **220** 567
[67] Giannozzi P *et al* 2009 *J. Phys.: Condens. Matter.* **21** 395502
[68] Pashov D, Acharya S, Lambrecht W R L, Jackson J, Belashchenko K D, Chantis A, Jamet F and van Schilfgaarde M 2020 *Comput. Phys. Commun.* **249** 107065
[69] Asato M, Settels A, Hoshino T, Asada T, Blügel S, Zeller R and Dederichs P H 1999 *Phys. Rev.* B **60** 5202
[70] Larsen A H *et al* 2017 *J. Phys.: Condens. Matter.* **29** 273002
[71] Fischbacher J, Kovacs A, Gusenbauer M, Oezelt H, Exl L, Bance S and Schrefl T 2018 *J. Phys. D: Appl. Phys.* **51** 193002
[72] The MARMOT 2022 website https://warwick.ac.uk/marmotcode